

A Synaptic Transistor based on Quasi-2D Molybdenum Oxide

Chuan Sen Yang, Da Shan Shang,* Nan Liu, Gang Shi, Xi Shen, Ri Cheng Yu, Yong Qing Li, and Young Sun*

Biological synapses store and process information simultaneously by tuning the connection between two neighboring neurons. Such functionality inspires the task of hardware implementation of neuromorphic computing systems. Ionic/electronic hybrid three-terminal memristive devices, in which the channel conductance can be modulated according to the history of applied voltage and current, provide a more promising way of emulating synapses by a substantial reduction in complexity and energy consumption. 2D van der Waals materials with single or few layers of crystal unit cells have been a widespread innovation in three-terminal electronic devices. However, less attention has been paid to 2D transition-metal oxides, which have good stability and technique compatibility. Here, nanoscale three-terminal memristive transistors based on quasi-2D α -phase molybdenum oxide (α -MoO₃) to emulate biological synapses are presented. The essential synaptic behaviors, such as excitatory postsynaptic current, depression and potentiation of synaptic weight, and paired-pulse facilitation, as well as the transition of short-term plasticity to long-term potentiation, are demonstrated in the three-terminal devices. These results provide an insight into the potential application of 2D transition-metal oxides for synaptic devices with high scaling ability, low energy consumption, and high processing efficiency.

Biological synapses are functional links between neurons through which information is transmitted in the neuron network by sending and accepting neurotransmitters.^[1–3] The information can be stored and processed simultaneously in the same synapse through tuning the synaptic weight, which is defined as the strength of the correlation between two neighboring neurons, and the operation is collective and adaptive.^[4] This particular functionality of the synapse, called synaptic plasticity in neuroscience, provides a more effective way for information processing than that in traditional computers based on von Neumann architecture, in which memory and processing units are separated physically.^[5] Silicon-based complementary metal–oxide–semiconductor (CMOS) circuits have

been developed to emulate synaptic functions.^[6–8] However, this has faced significant challenges in large-scale integrations. One is circuit complexity, because the human brain is composed of neuronal networks connected by $\approx 10^{15}$ synapses, and each synapse requires at least ten transistors to mimic synapse function. Another is the huge energy consumption, which may be a millionfold higher than the energy of a biological synapse ($\approx fJ$) to implement a simple signal-transmission action between neurons. Memristive devices, in which the conductance can be retained according to the history of applied voltage and current,^[9–11] provide a more promising way to emulate synapses with a substantial reduction in complexity and energy consumption.^[12–19] In general, signal transmission and learning are performed at the same time in brain synapses. However, because the memristive devices are commonly a two-terminal component, the signal transmission and learning functions could not be

carried out simultaneously because the signal transmission is inhibited during the learning operation in which the output signal is fed back to the synaptic device. Therefore, complete emulation of the natural synapse is limited.^[20] Recently, ionic/electronic hybrid three-terminal memristive devices have been introduced,^[21–25] where the signal transmission is carried via the channel and the synaptic weights are modulated independently via the gate terminals; that is, the signal transmission and learning function can be performed simultaneously. This provides more flexible operation for the signal processing and learning in synaptic circuits. Thus, to build artificial neuromorphic networks with high scaling ability, low energy consumption, and high operation efficiency, nanoscale three-terminal synaptic devices are desirable.

2D van der Waals materials, with a single or few layers of crystal unit cells, have become the fertile soil for exploring unique physical and chemical properties since the emergence of graphene.^[26] By now, the 2D transition-metal dichalcogenides (TMDCs), in particular MoS₂, have been the most widely studied as 2D semiconducting materials for applications in electronic,^[27] optoelectronic,^[28] spin-electronic,^[29] thermoelectric,^[30] and flexible electronic devices.^[31,32] In contrast, less attention has been paid to 2D transition-metal oxides (TMOs) for their generally wider bandgap and low carrier concentration in stoichiometric states.^[33] Nevertheless, these properties

C. S. Yang, Dr. D. S. Shang, N. Liu, G. Shi, Dr. X. Shen, Prof. R. C. Yu, Prof. Y. Q. Li, Prof. Y. Sun
Beijing National Laboratory for Condensed Matter Physics
Institute of Physics
Chinese Academy of Sciences
Beijing 100190, P. R. China
E-mail: shangdashan@iphy.ac.cn; youngsun@iphy.ac.cn

 The ORCID identification number(s) for the author(s) of this article can be found under <http://dx.doi.org/10.1002/adma.201700906>.

DOI: 10.1002/adma.201700906

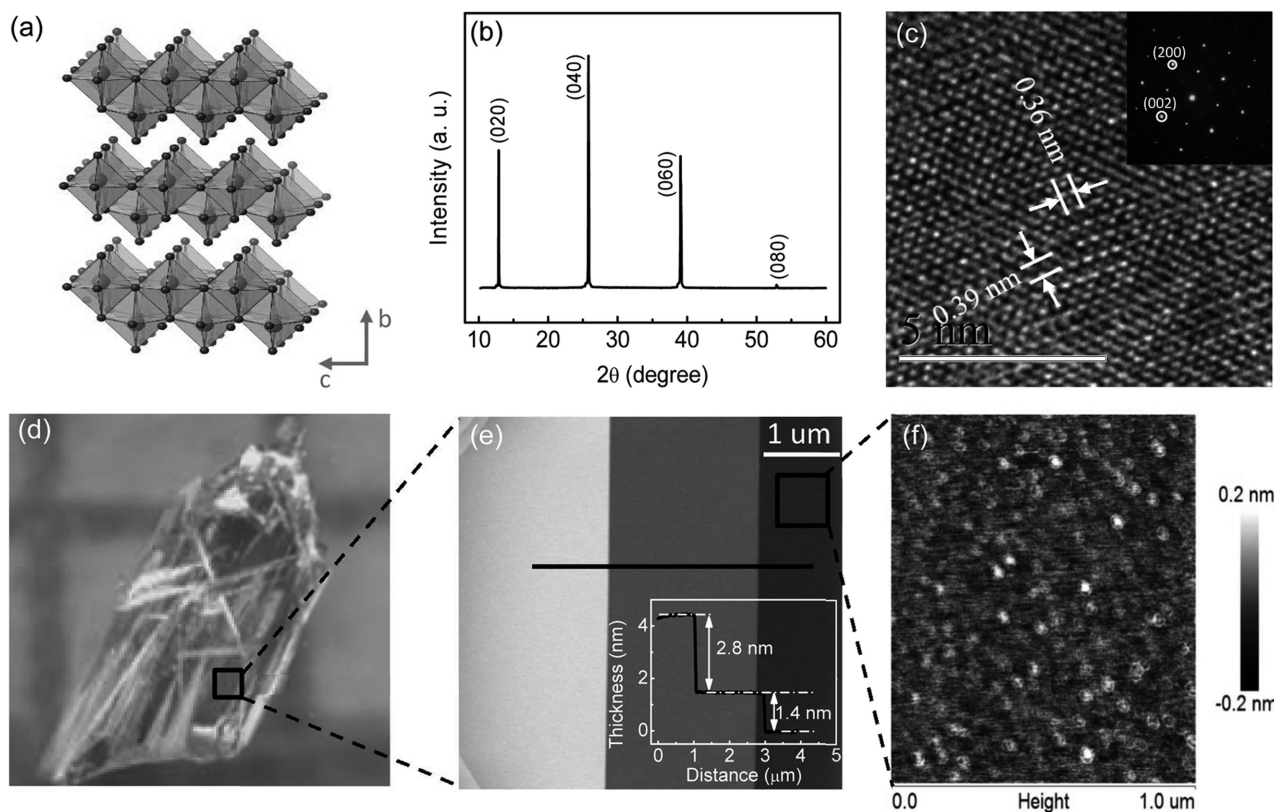


Figure 1. a) Crystal structure of α - MoO_3 . The structural framework consists of a bilayer network of edge-sharing MoO_6 octahedral structures. The lattice constants are $a = 3.963 \text{ \AA}$, $b = 13.856 \text{ \AA}$, and $c = 3.697 \text{ \AA}$. b) XRD pattern of the as-grown α - MoO_3 single crystal. c) HRTEM image of the α - MoO_3 nanoflake (the scale bar represents 5 nm). The inset shows the corresponding SAED. d) The optical image of the α - MoO_3 flake. e) Topography of the α - MoO_3 single-crystal surface measured by AFM. Inset: The line profile of the α - MoO_x nanoflake. f) AFM characterization of the plane depicted by the red rectangle in (e).

could find potential applications for the channel materials in three-terminal transistors to avoid excessive current and energy consumption. Moreover, compared with graphene and 2D dichalcogenides, TMOs are generally more stable and have good compatibility with the complementary metal–oxide–semiconductor technology. A typical 2D TMO is α -phase molybdenum oxide (α - MoO_3). Its crystal structure is layered by double sheets of MoO_6 octahedra, wherein each molybdenum atom bonds to edge-sharing, corner-sharing, and unshared terminal oxygen atoms (see **Figure 1a**). The layered structure of α - MoO_3 facilitates the intercalation of different cations (commonly protons and alkali metal ions) into the layer spacing, which gives rise to a multitude of interesting properties, such as gas sensing,^[34,35] biosensing,^[36] electrochromism,^[37] energy storage,^[38,39] optoelectronic devices,^[40,41] and resistive switching devices.^[42] These physical and chemical characteristics provide a chance to design ionic/electronic hybrid three-terminal devices using α - MoO_3 for artificial synapses.

Herein, we investigated a lateral three-terminal transistor based on quasi-2D α - MoO_3 in the ambient atmosphere, and capitalized on the nanoscale device to mimic a biological synapse. This work represents the first example of applying quasi-2D α - MoO_3 to an artificial synapse. An ionic liquid (IL) was selected as the gate terminal, serving as the presynaptic neuron to generate and control protons (neurotransmitters). The

ultrathin α - MoO_3 single-crystal flake serves as the postsynaptic neuron, whose conductance can be modulated by the IL. The excitatory postsynaptic current (EPSC), depression and potentiation of the synaptic weight, paired-pulse facilitation (PPF), and the transition of short-term plasticity (STP) to long-term potentiation (LTP) have been demonstrated in the three-terminal devices. These results provide an insight into the potential application of 2D TMOs for synaptic devices with high scaling ability, low energy consumption, and high processing efficiency.

We prepared highly homogenous single-crystal α - MoO_3 by the vapor-phase-transport method (see the Experimental Section for details). As shown in **Figure 1b**, the X-ray diffraction (XRD) pattern barely shows a series of sharp peaks at $2\theta = 12.9^\circ$, 25.8° , 39.1° , and 52.9° , which correspond to the (020), (040), (060), and (080) planes of α - MoO_3 (JCPD: 05-0508), respectively.^[43] **Figure 1c** shows the high-resolution transmission electron microscopy (HRTEM) image of the quasi-2D nanoflakes. Two sets of parallel lines indicate lattice constants of 0.39 and 0.36 nm, respectively, which correspond to the (100) and (001) lattice planes of α - MoO_3 . The corresponding selected area electron diffraction (SAED) pattern (see the inset of **Figure 1c**) shows a rectangular position of diffraction spots, indicating the orthorhombic lattice. The optical image of an as-grown single crystal with dimensions of a few millimeters in length/width and 0.5 mm in thickness is shown in **Figure 1d**. The crystal

is transparent with a large number of step-shaped features on the surface. The details of the step-shaped texture revealed by atomic force microscopy (AFM) are shown in Figure 1e. The steps, with thicknesses of 1.4 and 2.8 nm, show a fundamental thickness of 1.4 nm, which essentially corresponds to the magnitude of the α -MoO₃ lattice constant, $b = 1.389$ nm. The morphology of the plain of a single step indicates that the crystal has an atomic scale flat with a roughness of less than 0.2 nm (see Figure 1f).

To fabricate lateral three-terminal transistor devices using quasi-2D α -MoO₃, a mechanical-exfoliation method was used for the as-grown α -MoO₃ single crystals to obtain ultrathin α -MoO₃ nanoflakes on a SiO₂ (300 nm)/Si substrate (see the Experimental Section for details). A typical single-crystal nanoflake with a thickness of 12.6 nm (corresponding to nine double sheets) was selected (see Figure S1a, Supporting Information). The contacts for the lateral three-terminal devices were patterned by electron-beam lithography (EBL) and Cr/Au (5 nm/60 nm) contact electrodes were deposited via thermal evaporation. Then, the devices were annealed in vacuum ($<10^{-5}$ Torr) at 200 °C for 1 h in order to remove the resist residues and enhance the metallic contacts. Current–voltage measurements were performed to test the contact quality. The linear current–voltage relationship indicates good ohmic contacts under the electrodes (see Figure S1b, Supporting Information). Then, the ionic liquid 1-ethyl-3-methylimidazolium bis-(trifluoromethanesulfonyl)-imide (EMIM-TFSI) (Solvionic Co.) was dropped on top of the device as the gate terminal, as shown in Figure 2a. Figure 2b shows the schematic illustration of the device structure and measurement setup. A small dc voltage ($V_D = 50$ mV) was applied between the source and drain electrodes, and the corresponding drain current (I_D) was monitored. Meanwhile, the gate voltage (V_G) was directly applied on the gate electrode, and the corresponding gate leakage current (I_G) was also monitored.

The I_D and I_G dependence values of V_G were measured simultaneously at room temperature in ambient atmosphere with different relative humidity (RH) levels. Prior to the measurement, the sample was put into an enclosed chamber and baked under vacuum ($<10^{-4}$ Torr) at 100 °C for 3 h to minimize the influence of stray water in IL. After baking, the I_D – V_G curves of the sample were first measured under vacuum, and then were measured in the atmosphere with different RH levels, which were obtained by the saturated-salt-solution method (see the Experimental Section for details). Figure 2c shows the I_D – V_G curves with V_G sweeping at a rate of 20 mV s⁻¹. Under vacuum, the I_D – V_G curve showed a tiny hysteresis with the highest/lowest conductance ratio less than 3%. However, obvious I_D – V_G hysteresis appeared for RH = 18.6%. With an increase of RH, the amplitudes of the I_D – V_G hysteresis became significantly larger, and the highest/lowest conductance ratio reached 340% for RH = 45.1%. This large hysteresis indicates a potential functionality of the device for synapse emulation, which will be discussed later. Figure 2d shows the simultaneously monitored I_G . With the increase of RH, the I_G increased ≈ 2 orders of magnitude. Nevertheless, the value of I_G is still several orders smaller than that of I_D measured under vacuum, indicating the negligible effect of I_G on the performance of the three-terminal devices. The dramatically different

gate responses in different RH ambiances strongly indicate that the ambient water molecules, which may be adsorbed by the IL gate, play a crucial role in modifying the conductance of the MoO₃ nanoflake.

ILs have been widely studied for the use of electrolyte gating to induce extremely large modulations in the carrier densities at the interface between the IL and a wide variety of materials.^[44–46] The remarkable capability for carrier modulation is due to the formation of an electric double layer (EDL) at the IL/solid interface. However, the very weak change of I_D with V_G sweeping in vacuum indicates that the EDL, if it forms, has little effect on the carrier density of the channel. This might be due to the wide bandgap and low carrier density in the α -MoO₃ nanoflakes. In contrast, the dramatically different gate response of the channel conductance has been observed under different ambient RH levels. Similar humidity dependence of the electric-field-induced conductance change has also been observed in two-terminal memristive devices based on SiO₂, Ta₂O₅, Al₂O₃, MoO₃, and SrTiO₃.^[47–52] It has been demonstrated that ambient water molecules can penetrate into the oxide films and have an essential effect on the memristive switching property. It has been known that water molecules are apt to be adsorbed by ILs and then electrostatically dissociate into protons and hydroxyls,^[54] both of which have smaller ion sizes and relatively high chemical reactivity. In such cases, the H₂O-doped IL, also called a protic ionic liquid (PIL),^[55] might serve not only as the gate dielectric but also as a water electrolysis cell for the supply of protons and hydroxyls. Taking the layered structure of α -MoO₃ into account, we suggest that the large I_D – V_G hysteresis in the MoO₃ flake gated by the IL is related closely to the electrochemical doping process induced by the proton diffusion into the α -MoO₃ lattice.

Figure 2e shows a schematic illustration of the electric-field-induced ionic separation in the IL and the electrochemical proton-doping process. Here, the IL ions, such as EMI⁺ and FSI⁻, are ignored since the EDL induced by their accumulation has little effect on the I_D . The positive V_G attracts the hydroxyls toward the Au gate electrode and repels the protons toward the IL/ α -MoO₃ interface, resulting in a proton-rich region at the IL/ α -MoO₃ interface. It has been reported that there are two types of diffusion energy barriers governing the proton-doping into α -MoO₃, that is, the surface diffusion and bulk diffusion energy barriers, respectively. The surface diffusion energy barrier is ≈ 80 meV, while the bulk diffusion barrier is much smaller.^[56] Therefore, the accumulated protons are first adsorbed on the oxygen sites at the topmost layer of the α -MoO₃ nanoflake. With increasing gate voltage, parts of the protons overcome the surface diffusion barrier and diffuse into the α -MoO₃ lattice in conjunction with the charge transfer from the IL to Mo⁶⁺, which can be described by the following reaction:



This behavior is defined as electrochemical doping, where the valence of Mo⁶⁺ changes to Mo⁵⁺ with the formation of (Mo–O)–H bonds, that is, molybdenum bronze (H_xMoO₃). This reaction introduces external electron charges in the conduction band of α -MoO₃, resulting in an increase of the free electron density in the channel.^[57] Therefore, the I_D increases

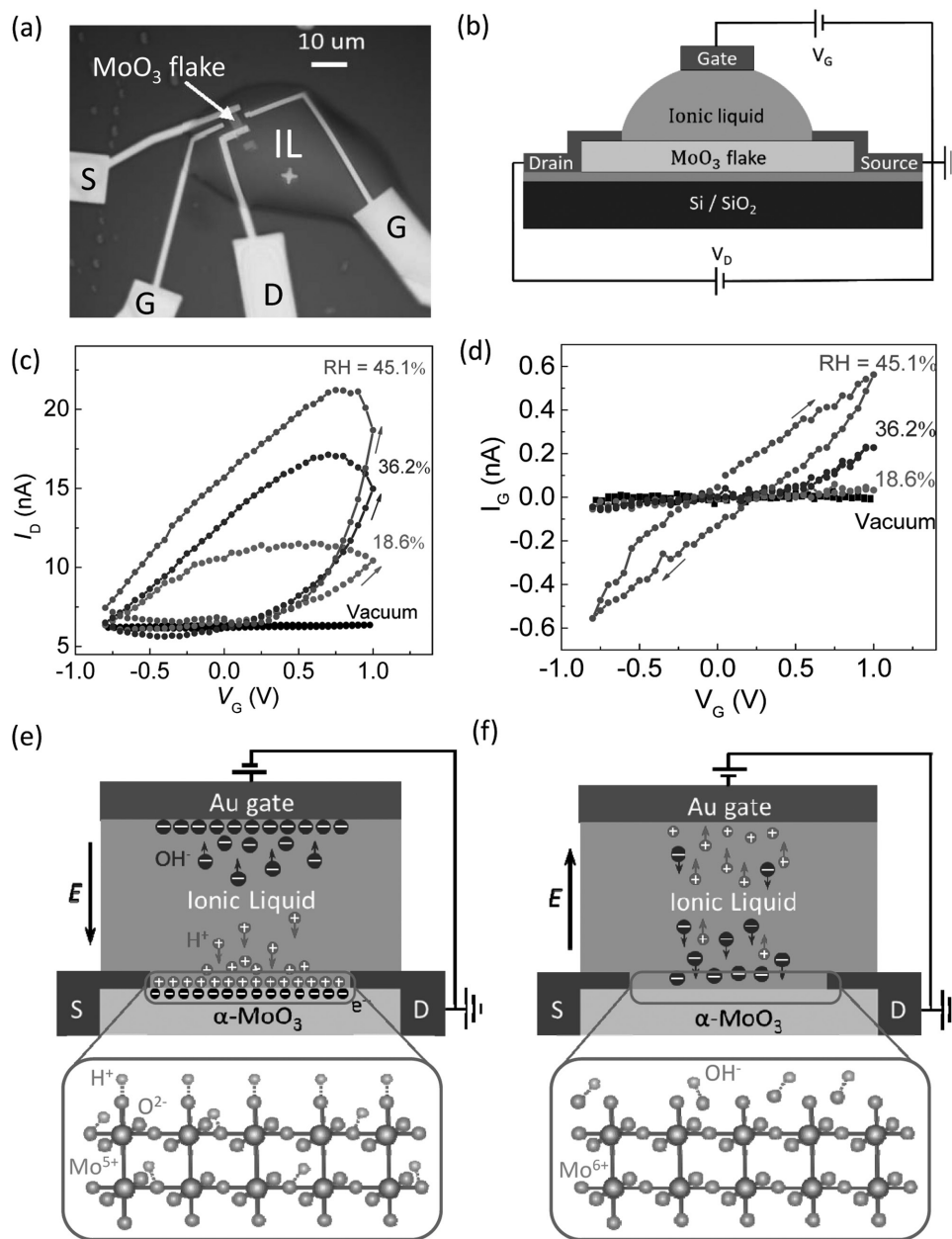


Figure 2. a) The optical image of the quasi-2D α -MoO₃-based three-terminal synaptic device. b) The schematic illustration of the device structure and measurement setup. A small dc voltage ($V_D = 50$ mV) was applied between the source and drain electrodes, and the corresponding drain current (I_D) was measured. The gate voltage (V_G) was directly applied on the gate electrode and the corresponding gate current (I_G) was also monitored. c,d) The I_D and I_G dependence of the gate voltage, respectively, under different relative humidity conditions (vacuum, 18.6%, 36.2%, 45.1%). e) Schematic of the transistor structure corresponding to the positive gate voltage application. The applied electric field drives the protons and hydroxyls, which dissociate from H₂O adsorbed in the ionic liquid, in the opposite direction. The protons are adsorbed at the α -MoO₃ channel surface and then injected into the α -MoO₃ lattice, resulting in the channel conductance increase. f) Schematic of the transistor structure corresponding to the negative gate voltage application. The protons are extracted and desorbed from the α -MoO₃ channel surface with the accumulation of hydroxyls, resulting in the channel conductance decrease back to the initial state.

largely under the positive V_G conditions. Note that the reported half-potential for the electrochemical reduction represented in Equation (1) is ≈ -0.41 and -0.49 V versus the saturated calomel electrode in 2×10^{-3} M H₂SO₄.^[58] However, because the electric measurements were performed without a reference electrode, the starting point of the half-cell reaction cannot be assigned. Therefore, we determine it just according to the fact

that I_D - V_G hysteresis is only visible in the atmosphere with humidity. As the gate voltage is reduced from its upper limit (1 V), the internal field built by the concentration gradient of ions in the IL becomes gradually dominant and drives the protons (hydroxyls) toward the Au/IL interface (IL/MoO₃ interface). Since the (Mo-O)-H bonding is so thermodynamically stable, a large desorption activation energy, namely, a large negative

V_G , is required to extract the protons from the α -MoO₃ channel, causing the large hysteresis in the I_D - V_G curves (see Figure 2c). When the V_G scans to a higher negative value (-1 V), protons diffuse out of the α -MoO₃ channel, with hydroxyls accumulating near the IL/ α -MoO₃ interface (see Figure 2f), and then I_D is restored to the initial value. The enhancement of the I_D - V_G hysteresis with the increasing RH level can be attributed to the electrochemical reaction rate dependence on proton concentration. We suggest that the proton concentration is related to the RH level of the ambient atmosphere. With the increasing RH level, more water molecules are adsorbed by the ionic liquid gate, resulting in the increase of proton concentration in the ionic liquid gate, that is, the increase of the ionic liquid acidity. Then, according to the Nernst equation,^[59] the overpotential of Equation (1) becomes larger, and the electrochemical reduction rate is increased under the fixed sweep rate of the gate voltage. Therefore, the I_D - V_G hysteresis becomes larger with the increasing RH level.

To verify the electrochemical proton-doping process, micro-Raman spectra of the α -MoO₃ nanoflake for different gating times were measured. As shown in Figure 3a, the SiO₂/Si substrate signals always appear as a broad flat band that covers the area from 930 to 1000 cm⁻¹, and the strongest peak at 520 cm⁻¹ was skipped in the measurement because its

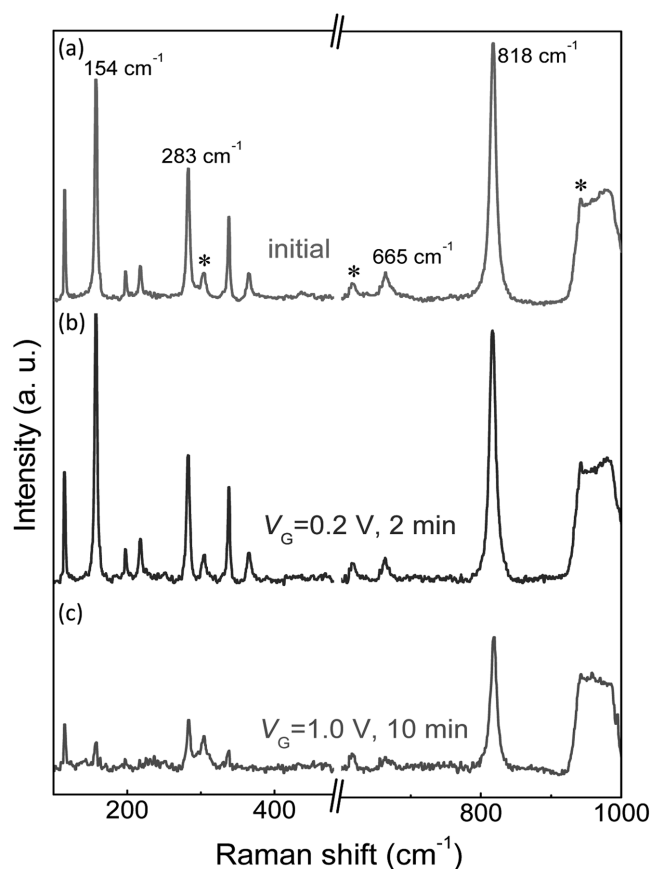


Figure 3. Evolution of the Raman spectra of the α -MoO₃ channel after undergoing gate voltage stimulation. The gate voltage (V_G) and gating time are labeled above the spectra. a) The initial state, b) gated by $V_G = 0.2$ V for 2 min, and c) gated by $V_G = 1$ V for 10 min.

intensity was outside the upper limit of the detector. For the pristine state of the device, the typical 115, 154, 198, 217, 283, 338, 365, 665, and 818 cm⁻¹ peaks corresponding to the A_g, B_{1g}, and B_{3g} modes of the α -MoO₃ were observed.^[43,57] After applying the gating voltage ($V_G = 0.2$ V) in ambient conditions (RH = 45.1%) for 2 min, there was almost no change compared with the pristine state, indicating that merely contacting with the IL and gating with low bias have no effect on the crystal structure of the α -MoO₃. After increasing the V_G to 1 V and applying it for 10 min, the intensity of all the α -MoO₃ modes decreased significantly with little change in the Si modes. This change in the trend is exactly consistent with the hydrogenation process of MoO₃ in a hydrogen environment and can be attributed to electronic screening of phonons as a result of electrons induced by the electrochemical doping.^[60] We have also measured the micro-Raman spectra of the α -MoO₃ nanoflake gated by 2.5 V for 30 and 90 min, respectively. Almost all the Raman modes of α -MoO₃ disappeared (see Figure S2a, Supporting Information). After applying negative gate voltage, the Raman modes cannot be restored to the initial state. This phenomenon has been observed in the hydrogenation process of MoO₃ with high hydrogen concentration^[56,60,61] and can be explained by the deformation of the α -MoO₃ lattice, which experiences the following three steps (see Figure S2b, Supporting Information). First, with increasing gating voltage, the absorbed protons overcome the surface diffusion barrier and diffuse into the α -MoO₃ lattice, leading to the electrochemical doping (Equation (1)). Second, as the proton concentration increases, the oxygen ions bridging the two octahedral are bonded with two protons to form -OH₂ groups. Third, as the concentrations of the -OH₂ group increase, local strain becomes strong enough to release the H₂O molecules, leaving the oxygen vacancy defects and then resulting in the decomposition of H_xMoO₃ into MoO₂ and H₂O. MoO₂ is a metallic conductor. Although the formation of MoO₂ further increases the channel conductance, it should be noted that the decomposition of H_xMoO₃, that is, the long duration gating under high voltage, should be avoided in view of its application in synaptic devices because, in this case, the conductivity of the channel cannot return to the pristine state by applying negative V_G ; that is, the modulation of the channel conductivity becomes irreversible.

The gating-controlled reversible electrochemical doping process closely resembles the transmission process of chemical messengers in biological synapses. Figure 4a shows a schematic illustration of chemical messengers transmitting in a biological synapse which is a conjunction of two neighboring neuron cells (presynaptic and postsynaptic neuron). The information transmits between neurons by sending neurotransmitters from the presynaptic neuron to the postsynaptic neuron. If an appropriate charge is sent down to the presynaptic neuron and changes the voltage level of the Ca²⁺ channel, the neurotransmitters are released and go across the synapse to dock with receptors on the postsynaptic neuron. If enough neurotransmitters dock with the receptors, a signal is sent down that neuron. When the signal fades, the neurotransmitters are released from receptors and taken up into the synaptic vesicle of the presynaptic neuron by a re-uptake transporter. That means, under external stimulus, spikes or action potentials

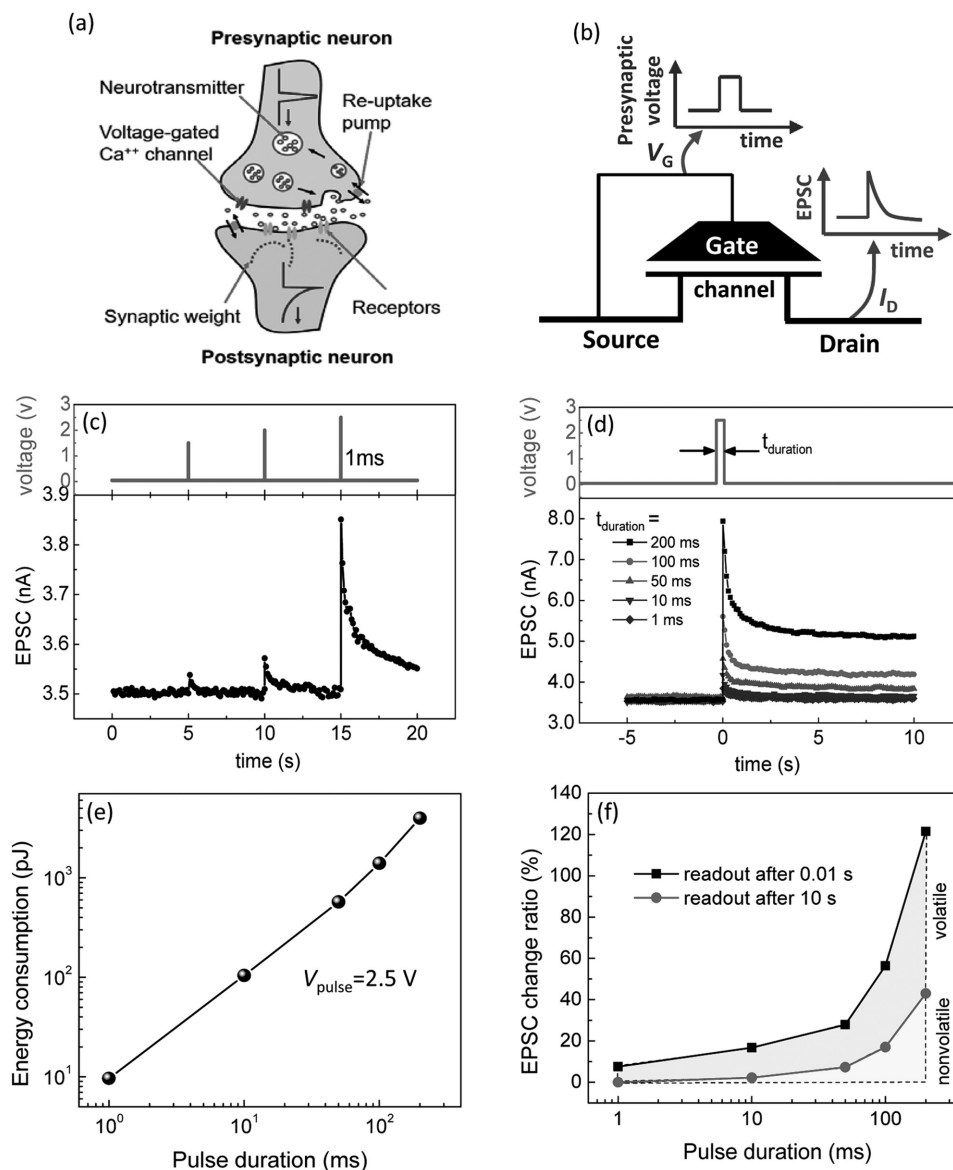


Figure 4. a) Schematic illustration of a biological synapse. In a synapse, the arrival of an action potential releases neurotransmitters that assist ion channels for signal transmission. b) Schematic diagram of the three-terminal synaptic transistor, in which the source and drain are used as the postsynaptic output terminals. A presynaptic voltage applied on the gate will trigger an EPSC in the α -MoO₃ channel. c) EPSC triggered by a series of presynaptic pulses with the same duration time (1 ms) and different amplitudes (1.5, 2.0, and 2.5 V). d) EPSCs triggered by a presynaptic pulse with different pulse durations. The pulse amplitude was fixed at 2.5 V. e) Pulse duration dependence of the energy consumption for a single pulse event. f) Pulse-duration dependence of the EPSC change ratio, $((I - I_0)/I_0) \times 100\%$. I_0 and I are the initial drain current and the drain current after the gate voltage pulse stimulation, respectively.

from the presynaptic neuron can be transmitted through the synapse to the postsynaptic neuron and generate an excitatory postsynaptic current (EPSC), whose amplitudes or intensity are determined by the connection strength, that is, the synaptic weight. Herein, the synaptic behavior can be emulated by the α -MoO₃-based three-terminal transistor. The conductance of the α -MoO₃ nanoflake channel will be considered as the synaptic weight, which can be tuned by the gating voltage, that is, the presynaptic voltage. The application of the presynaptic voltage on the in-plane gate electrode can trigger an EPSC in the α -MoO₃ nanoflake channel (see Figure 4b).

Figure 4c shows the EPSC responses of the α -MoO₃-based synaptic transistor at room temperature in ambient conditions (RH = 45.1%). A series of presynaptic pulses with the same duration time (1 ms) and different amplitudes (1.5, 2.0, and 2.5 V) were applied on the IL gate electrode, and a fixed source–drain voltage ($V_D = 50$ mV) was applied for the EPSC measurement. The EPSC shows a sudden increase after applying the presynaptic pulse and decays back gradually to the resting current (3.5 nA). The EPSC peak value increases systematically with increasing amplitudes of presynaptic pulses from 3.53 nA for 1.5 V to 3.85 nA for 2.5 V. Such EPSC

behavior is quite similar to that in a biological excitatory synapse. Figure 4d shows the EPSC induced by presynaptic pulses with different durations. The amplitudes of the EPSCs increase from 3.85 to 7.94 nA with increasing the pulse duration time from 1 to 200 ms. The energy consumption for a single pulse event is defined as $I_{\text{peak}} \times t \times V_{\text{D}}$, where I_{peak} , t , and V_{D} are the peak value of the EPSC, the pulse duration time, and the drain voltage, respectively. The calculated values of energy consumption for a single pulse with different duration times are shown in Figure 4e. The energy consumption is reduced rapidly with the reduction of the pulse duration time. The smallest value is estimated to be 9.6 pJ (2.5 V, 1 ms), which is about two orders of magnitude lower than that of the conventional CMOS circuit (≈ 900 pJ per stimulation),^[6,61] and comparable to that of reported three-terminal artificial synaptic devices.^[22–25] It is reasonable to expect that the energy consumption of our devices can be further reduced by decreasing the pulse duration to a sub-millisecond level. Moreover, with increasing pulse duration time, the EPSC cannot decay back to the resting current during the measurement period (10 s), indicating a significant memory behavior of the conductivity change of the α -MoO₃ channel. The pulse duration-dependent memory behavior can be understood based on the electrochemical proton adsorption and proton-doping process in the α -MoO₃ channel, as shown schematically in Figure S3 (Supporting Information). Driven by the positive gate voltage, protons in the IL are first adsorbed at the α -MoO₃ surface, forming O–H bonds with the topmost oxygen ions and providing additional charge carriers in the channel. When removing the gate voltage, the adsorbed protons are gradually desorbed by the internal electric field induced by the ion concentration gradient in IL, resulting in the decay of EPSC to the resting value, that is, a short-term memory effect of the channel conductance change. When increasing the duration time of the positive gate voltage, a portion of the protons have the chance to overcome the surface diffusion energy barrier and diffuse into the α -MoO₃ bulk, forming (M–O)–H bonds, as is defined as the electrochemical proton-doping process (Equation (1)). In such a situation, the injected protons cannot be extracted by the internal field after removing the gate voltage due to the thermodynamic stability of (Mo–O)–H bonds in α -MoO₃, leading to a long-term memory effect of the channel conductance change.

The efficiency of the human brain depends on synaptic plasticity, which is the biological basis for the brain to learn, memorize, and forget. A prominent characteristic of synaptic plasticity is the presence of STP and LTP, separated by the retention times of the synaptic weight. Additionally, a transition from STP to LTP can be achieved after sufficient training, which provides a very practical application in allocating limited sources for the most efficient use during operation.^[13,62] The short- and long-term memory effect of the channel conductance in the α -MoO₃-based synaptic transistor can be used to emulate the STP and LTP characteristics.

PPF is an important short-term synaptic plasticity, which is essential to decode temporal information in auditory or visual signals.^[14,24,63] PPF depicts the phenomenon that occurs when two consecutive presynaptic pulses are applied. The amplitude of EPSC generated by the second pulse is larger than that of the first pulse and is determined by the time interval between the two pulses; that is, a smaller interval will lead to a larger EPSC

amplitude enhancement. PPF property can also be emulated by the α -MoO₃-based synaptic transistor. Figure 5a shows the EPSC generated by a pair of presynaptic pulses (2.5 V, 1 ms) with a pulse interval (Δt) of 2 s. It can be seen clearly that the amplitude of the EPSC generated by the second presynaptic pulse is larger than that of the first one. The PPF can be manifested by the ratio between the EPSC measured immediately after the first pulse (I_{D1}) and the second pulse (I_{D2}), that is, PPF index $((I_{\text{D2}} - I_{\text{D1}})/I_{\text{D1}}) \times 100\%$. Figure 5b shows that the dependence of the EPSC enhancement on the pulse interval follows two-phase behavior, which can be fitted well by a double-exponential function:

$$\text{PPF} = 1 + C_1 \exp\left(-\frac{t}{\tau_1}\right) + C_2 \exp\left(-\frac{t}{\tau_2}\right) \quad (2)$$

where t is the pulse interval time, C_1 and C_2 are the initial facilitation magnitudes of the respective phases, and τ_1 and τ_2 are the characteristic relaxation times of the respective phases. In the fitting, $C_1 = 9.2\%$, $C_2 = 8.0\%$, $\tau_1 = 72$ ms, and $\tau_2 = 3388$ ms. The characteristic relaxation time of the short-term and long-term phases of the synaptic transistor is comparable in scale to those of a biological synapse.^[24,64,65]

The PPF behavior can be explained by the adsorption/desorption of the protons at the α -MoO₃ surface. When the pulse interval is shorter than the desorption time, the protons adsorbed by the first pulse cannot be fully desorbed from the α -MoO₃ surface by the internal field. Therefore, if the second pulse is applied, the proton adsorption is enhanced with the residual adsorbed protons, and then the channel current is facilitated. Based on this scenario, it can be expected that more and more protons will be adsorbed at the α -MoO₃ lattice with increasing gate voltage pulse numbers, achieving a gradual modulation of the channel conductance (or synaptic weight).

Figure 5c,d shows the channel conductance modulation by applying 50 consecutive positive gate pulses (2.5 V for 1 ms spaced 200 ms apart). A small drain voltage ($V_{\text{D}} = 50$ mV) was applied to monitor the drain current. The drain current increases continuously from 3.5 to 4.75 nA. Then, it is decreased to 3.5 nA again by applying 50 consecutive negative pulses (–1.85 V for 1 ms spaced 200 ms apart). In addition, the retention time of the conductance change is enhanced with increasing pulse number. Figure 5e shows the EPSC obtained by applying 10, 50, and 100 voltage pulses (2.5 V for 1 ms spaced 200 ms apart). The EPSC cannot decay back to the resting value after 50 s, indicating a long-term memory effect of the channel conductance change (i.e., synaptic plasticity). Figure 5f shows the calculated EPSC change ratio by comparing the I_{D} measured immediately (≈ 0.01 s) and 50 s after the pulse stimulation with the resting current (I_{D0}). The residual EPSC after 50 s is enhanced significantly with increasing pulse number, indicating a trend of transition from STP to LTP. This behavior can be understood in the view that more protons are injected into the α -MoO₃ lattice with increasing pulse numbers, attaining similar effects of increasing pulse duration (see Figure 4f). In the implementation of artificial synapses, the channel conductance increase and decrease can be used to emulate the potentiation and depression of synaptic weight, respectively. The results

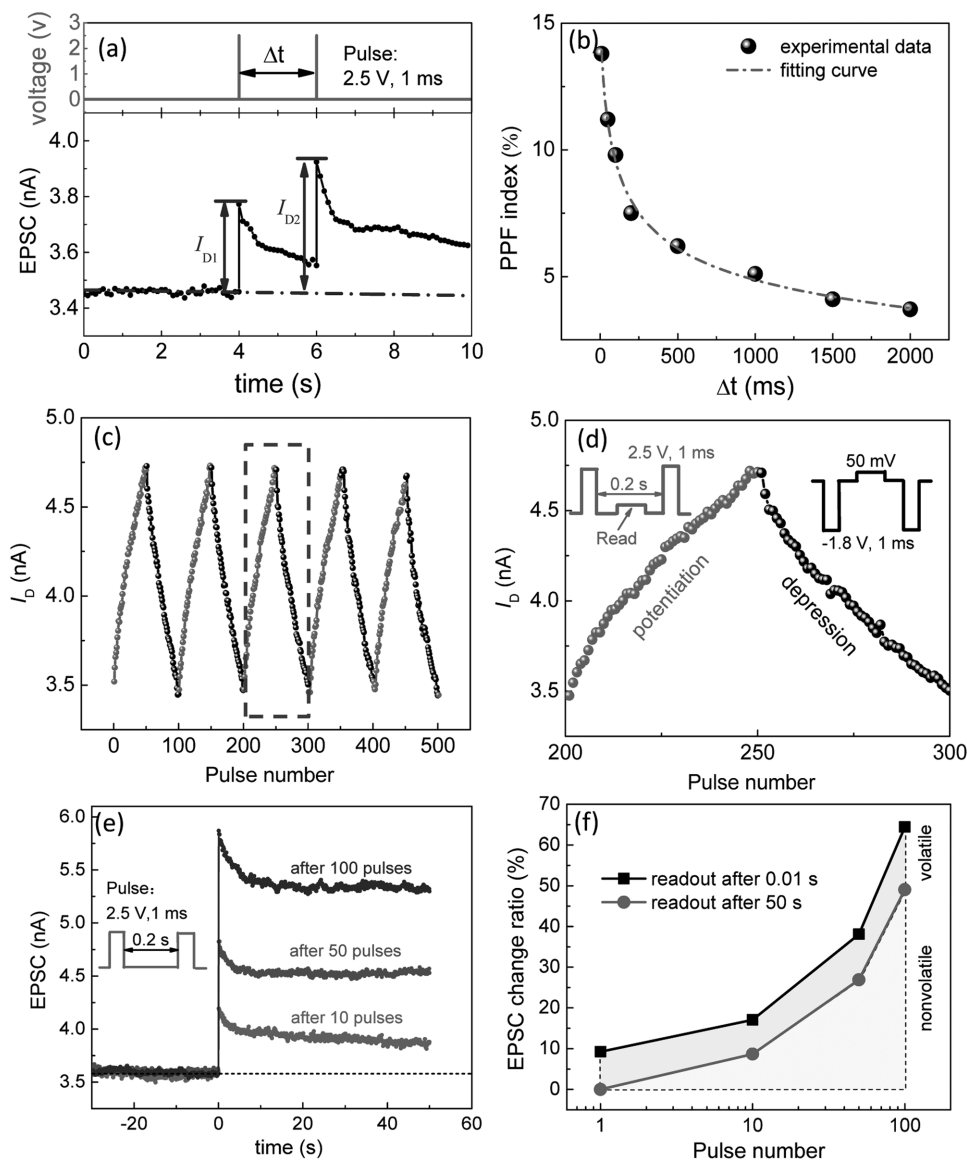


Figure 5. a) The EPSCs triggered by a pair of presynaptic pulses with a $\Delta t = 1000$ ms. I_{D1} and I_{D2} are the amplitudes of the first and second EPSCs, respectively. b) PPF index, defined as $((I_{D2} - I_{D1})/I_{D1}) \times 100\%$, plotted as a function of pulse interval, Δt , between two successive presynaptic pulses. c) Gradual channel current modulation under repeated positive (2.5 V for 1 ms spaced 200 ms apart) and negative (-1.8 V for 1 ms spaced 200 ms apart) gate voltage pulses. d) Enlargement of one of the cycles in (c). The channel current increase and decrease indicate the biological synaptic potentiation and depression, respectively. e) The EPSC decay after applying 10, 50, and 100 pulses (2.5 V for 1 ms spaced 200 ms apart). f) Dependence of the EPSC change ratio $[(I_D - I_{D0})/I_{D0}] \times 100\%$ on the pulse numbers. I_{D0} and I_D are the resting drain current and the drain current after the gate voltage pulse stimulation, respectively.

shown in Figure 5 demonstrate that the channel conductance can be set to numerous levels by an appropriate number of consecutive pulses with fixed voltage and width. This analog-like functionality is particularly appealing for the integration of the three-terminal devices in neuromorphic computational architectures. Some neuromorphic computational functions, such as spiking-time-dependent plasticity (STDP), spiking logic operation, and Pavlovian learning, have been successfully demonstrated in three-terminal synaptic transistors.^[22–25,66]

In summary, we have investigated three-terminal synaptic transistors based on quasi-2D α -MoO₃ nanoflakes for the first

time, and demonstrated that the IL gating-controlled electrochemical proton-doping is feasible to modulate the α -MoO₃ channel conductance in a reversible, nonvolatile way. The dynamic process of protons under gating voltage closely resembles the transmission of chemical signals in biological synapses. The essential functions of biological synapses have been demonstrated in the α -MoO₃-based transistors. These findings provide a clue to achieving conductivity modulation of 2D transition-metal oxides and pave a sensible way to the development of synaptic devices based on 2D molybdenum oxide.

Experimental Section

Synthesis of α -MoO₃ Crystal: α -MoO₃ single crystal was prepared by the vapor-transport method. A ceramic boat with 2 g of MoO₃ powder (99.9%, Alfa Aesar) and the glass substrate were placed in the center and the downstream end of a horizontal tube furnace, respectively. Then, the center of the tube furnace was heated to 720 °C at a rate of 5 °C min⁻¹ and maintained for 3 h in argon gas with a flow rate of 100 sccm s⁻¹, and the α -MoO₃ single crystal with dimensions up to a few millimeters in length/width, and 0.5 mm in thickness was collected at the edge of the glass substrate.

Mechanical Exfoliation of Few-Layered α -MoO₃ Nanoflakes: Scotch tape was attached to the as-prepared α -MoO₃ single crystal. After peeling it off the crystal, multilayer α -MoO₃ remained on the tape. By repeated peeling, the multilayer α -MoO₃ was cleaved into various flakes with few layers. After that, the tape was attached to the SiO₂ (300 nm)/Si substrate, which had been treated by plasma beforehand to increase the adhesion of the MoO₃ sheets. Then, the tape was peeled off swiftly, and a large number of MoO₃ flakes with thicknesses less than 20 nm were obtained.

Fabrication of the Synaptic Transistor Device: EBL was used to pattern the contacts of the α -MoO₃ flakes onto the 300 nm SiO₂/Si substrate to form lateral three-terminal devices. Cr/Au (5 nm/60 nm) contact electrodes were deposited via thermal evaporation. Then, the devices were annealed in vacuum (10⁻⁵ Torr) at 200 °C for 1 h in order to remove resist residues and enhance the metallic contacts. After that, the ionic liquid 1-ethyl-3-methylimidazolium bis-(trifluoromethanesulfonyl)-imide (Solvionic Co.) was dripped carefully on top of the device.

Characterization: The XRD was performed with a diffractometer (Rigaku Miniflex with copper K α). The HRTEM was performed with an electron microscope operated at 100 kV (JEOL 2100F). Raman spectra were measured using a micro-Raman spectrometer (Renishaw InVia microscope) with a 1200 lines mm⁻¹ blaze grating and a 1 mW laser excitation source at 514 nm. The laser beam was focused using a 50 \times objective with numeric aperture NA = 0.5, and the spot size was \approx 1.5 μ m. The electrical measurements were carried out on a home-made probe station in an enclosed chamber through two Keithley 2611 source meters. The relative humidity level was controlled by the saturated-salt-solution method. In an enclosed measurement chamber with a hygrometer mounted internally, excess LiCl, CH₃COOK, MgCl₂, and Mg(NO₃)₂ were dissolved in deionized water in a container to obtain the relative humidity levels of 18%, 33%, and 45%, respectively, at room temperature.^[51] Each relative humidity level needs to be stabilized for 3 h at least in the chamber before the electrical measurement. All the characterizations were performed at room temperature.

Supporting Information

Supporting Information is available from the Wiley Online Library or from the author.

Acknowledgements

This work was supported by the National Nature Science Foundation of China (Grant Nos. 51671213 and 11534015), the National Key Research Program of China (Grant No. 2016YFA0300701), and the Chinese Academy of Sciences (Grant Nos. XDB07030200 and KJZD-EW-M05). D.S. acknowledges the support from the Opening Project of the State Key Laboratory of High Performance Ceramics and Superfine Microstructure (Grant No. SKL201505SIC).

Conflict of Interest

The authors declare no conflict of interest.

Keywords

2D oxides, memristive systems, synaptic plasticity, synaptic transistors

Received: February 14, 2017

Revised: March 24, 2017

Published online:

- [1] E. R. Kandel, *Science* **2001**, 294, 1030.
- [2] S. N. Yang, Y. G. Tang, R. S. Zucker, *J. Neurophysiol.* **1999**, 81, 781.
- [3] H. Z. Shouval, M. F. Bear, L. N. Cooper, *Proc. Natl. Acad. Sci. USA* **2002**, 99, 10831.
- [4] D. S. Jeong, I. Kim, M. Ziegler, H. Kohlstedt, *RSC Adv.* **2013**, 3, 3169.
- [5] D. Kuzum, S. Yu, H. S. P. Wong, *Nanotechnology* **2013**, 24, 382001.
- [6] G. Indiveri, E. Chicca, R. Douglas, *IEEE Trans. Neural Networks* **2006**, 17, 211.
- [7] J. V. Arthur, K. Boahen, *IEEE Trans. Circuits Syst. I: Reg. Pap.* **2006**, 58, 1034.
- [8] S. Fusi, M. Annunziato, D. Badoni, A. Salamon, D. J. Armit, *Neural Comput.* **2009**, 12, 2227.
- [9] L. O. Chua, *IEEE Circuit Theory* **1971**, 18, 507.
- [10] D. B. Strukov, G. S. Snider, D. R. Stewart, R. S. Williams, *Nature* **2008**, 453, 80.
- [11] J. J. Yang, D. B. Strukov, D. R. Stewart, *Nat. Nanotechnol.* **2013**, 8, 13.
- [12] Z. H. Tan, R. Yang, K. Terabe, X. B. Yin, X. D. Zhang, X. Guo, *Adv. Mater.* **2015**, 28, 377.
- [13] T. Hasegawa, T. Ohno, K. Terabe, T. Tsuruoka, T. Nakayama, J. K. Gimzewski, M. Aono, *Adv. Mater.* **2010**, 22, 1831.
- [14] S. H. Jo, T. Chang, I. Ebong, B. B. Bhadviya, P. Mazumder, W. Lu, *Nano Lett.* **2010**, 10, 1297.
- [15] D. Kuzum, R. G. D. Jeyasingh, B. Lee, H. S. P. Wong, *Nano Lett.* **2012**, 12, 2179.
- [16] Z. Wang, S. Joshi, S. E. Savel'ev, H. Jiang, R. Midya, P. Lin, M. Hu, N. Ge, J. P. Strachan, Z. Li, Q. Wu, M. Barnell, G. L. Li, H. L. Xin, R. S. Williams, Q. Xia, J. J. Yang, *Nat. Mater.* **2017**, 16, 101.
- [17] A. Serb, J. Bill, A. Khiat, R. Berdan, R. Legenstein, T. Prodromakis, *Nat. Commun.* **2016**, 7, 12611.
- [18] R. Berdan, E. Vasilaki, A. Khiat, G. Indiveri, A. Serb, T. Prodromakis, *Sci. Rep.* **2016**, 6, 18639.
- [19] T. Tuma, A. Pantazi, M. L. Gallo, A. Sebastian, E. Eleftheriou, *Nat. Nanotechnol.* **2016**, 11, 693.
- [20] C. S. Yang, D. S. Shang, Y. S. Chai, L. Q. Yan, B. G. Shen, Y. Sun, *Phys. Chem. Chem. Phys.* **2017**, 19, 4190.
- [21] P. B. Phillai, M. M. De Souza, *ACS Appl. Mater. Interfaces* **2007**, 9, 1609.
- [22] J. Shi, S. D. Ha, Y. Zhou, F. Schoofs, S. Ramanathan, *Nat. Commun.* **2013**, 4, 2676.
- [23] L. Q. Zhu, C. J. Wan, L. Q. Guo, Y. Shi, Q. Wan, *Nat. Commun.* **2014**, 5, 3158.
- [24] Y. H. Liu, L. Q. Zhu, P. Feng, Y. Shi, Q. Wan, *Adv. Mater.* **2015**, 27, 5599.
- [25] F. Alibart, S. Pleutin, O. Bichler, C. Gamrat, T. Serrano-Gotarredona, B. Linares-Barranco, D. Vuillaume, *Adv. Funct. Mater.* **2012**, 22, 609.
- [26] K. S. Novoselov, A. K. Geim, S. V. Morozov, D. Jiang, Y. Zhang, S. V. Dubonos, I. V. Grigorieva, A. A. Firsov, *Science* **2004**, 306, 666.
- [27] B. Radisavljevic, A. Radenovic, J. Brivio, V. Giacometti, A. Kis, *Nat. Nanotechnol.* **2011**, 6, 147.
- [28] Z. Yin, H. Li, H. Li, L. Jiang, Y. Shi, Y. Sun, G. Lu, Q. Zhang, X. Chen, H. Zhang, *ACS Nano* **2012**, 6, 74.
- [29] H. Zeng, J. Dai, W. Yao, D. Xiao, X. Cui, *Nat. Nanotechnol.* **2012**, 7, 490.
- [30] J. Wu, H. Schmidt, K. K. Amara, X. Xu, G. Eda, B. Özyilmaz, *Nano Lett.* **2014**, 14, 2730.

- [31] Q. H. Wang, K. Kalantar-Zadeh, A. Kis, J. N. Coleman, M. S. Strano, *Nat. Nanotechnol.* **2012**, 7, 699.
- [32] D. Akinwande, N. Petrone, J. Hone, *Nat. Commun.* **2014**, 5, 5678.
- [33] M. M. Y. A. Alsaif, A. F. Chrimes, T. Daeneke, S. Balendhran, D. O. Bellisario, Y. Son, M. R. Field, W. Zhang, H. Nili, E. P. Nguyen, K. Latham, J. van Embden, M. S. Strano, J. Z. Ou, K. Kalantar-zadeh, *Adv. Funct. Mater.* **2016**, 26, 91.
- [34] O. Lupan, V. Cretu, M. Deng, D. Gedamu, I. Paulowicz, S. Kaps, Y. K. Mishra, O. Polonskyi, C. Zamponi, L. Kienle, *J. Phys. Chem. C* **2014**, 118, 15068.
- [35] M. B. Rahmani, S. H. Keshmiri, J. Yu, A. Z. Sadek, L. Al-Mashat, A. Moafi, K. Latham, Y. X. Li, W. Wlodarski, K. Kalantar-zadeh, *Sens. Actuators, B* **2010**, 145, 13.
- [36] S. Balendhran, S. Walia, M. Alsaif, E. P. Nguyen, J. Z. Ou, S. Zhuikov, S. Sriram, M. Bhaskaran, K. Kalantar-zadeh, *ACS Nano* **2013**, 7, 9753.
- [37] M. J. Wang, K. J. Koski, *ACS Nano* **2015**, 9, 3226.
- [38] P. Meduri, E. Clark, J. H. Kim, E. Dayalan, G. U. Sumanasekera, M. K. Sunkara, *Nano Lett.* **2012**, 12, 1784.
- [39] D. Hanlon, C. Backes, T. M. Higgins, M. Hughes, A. O'Neill, P. King, N. McEvoy, G. S. Duesberg, B. M. Sanchez, H. Pettersson, V. Nicolosi, J. N. Coleman, *Chem. Mater.* **2014**, 26, 1751.
- [40] H. Kanno, R. J. Holmes, Y. Sun, S. Kena-Cohen, S. R. Forrest, *Adv. Mater.* **2006**, 18, 339.
- [41] D. Xiang, C. Han, J. Zhang, W. Chen, *Sci. Rep.* **2014**, 4, 4891.
- [42] Z. H. Tan, X. B. Yin, X. Guo, *Appl. Phys. Lett.* **2015**, 106, 023503.
- [43] K. Kalantar-zadeh, J. S. Tang, M. S. Wang, K. L. Wang, A. Shailos, K. Galatsis, R. Kojima, V. Strong, A. Lech, W. Wlodarski, R. B. Kaner, *Nanoscale* **2009**, 2, 429.
- [44] K. Ueno, S. Nakamura, H. Shimotani, A. Ohtomo, N. Kimura, T. Nojima, H. Aoki, Y. Iwasa, M. Kawasaki, *Nat. Mater.* **2008**, 7, 855.
- [45] J. T. Ye, S. Inoue, K. Kobayashi, Y. Kasahara, H. T. Yuan, H. Shimotani, Y. Iwasa, *Nat. Mater.* **2010**, 9, 125.
- [46] J. Jeong, N. Aetukuri, T. Graf, T. D. Schladt, M. G. Samant, S. S. P. Parkin, *Science* **2013**, 339, 1402.
- [47] T. Tsuruoka, K. Terabe, T. Hasegawa, I. Valov, R. Waser, M. Aono, *Adv. Funct. Mater.* **2012**, 22, 70.
- [48] S. Tappertzhofen, I. Valov, T. Tsuruoka, T. Hasegawa, R. Waser, M. Aono, *ACS Nano* **2013**, 7, 6396.
- [49] M. Lübben, P. Karakolis, V. Ioannou-Sougleridis, P. Normand, P. Dimitrakis, I. Valov, *Adv. Mater.* **2015**, 27, 6202.
- [50] N. Knorr, A. Bamedi, Z. Karipidou, R. Wirtz, M. Sarpasan, S. Rosseli, G. Nelles, *J. Appl. Phys.* **2013**, 114, 124510.
- [51] C. S. Yang, D. S. Shang, Y. S. Chai, L. Q. Yan, B. G. Shen, Y. Sun, *Phys. Chem. Chem. Phys.* **2016**, 18, 12466.
- [52] F. Messerschmitt, M. Kubicek, J. L. M. Rupp, *Adv. Funct. Mater.* **2015**, 25, 5117.
- [53] T. L. Greaves, C. J. Drummond, *Chem. Rev.* **2008**, 108, 206.
- [54] K. Fumino, A. Wulf, R. Ludwig, *Angew. Chem., Int. Ed.* **2009**, 48, 3184.
- [55] W. Xie, M. Su, Z. Zheng, Y. Wang, L. Gong, F. Xie, W. Zhang, Z. Luo, J. Luo, P. Liu, N. Xu, S. Deng, H. Chen, J. Chen, *ACS Nano* **2016**, 10, 1662.
- [56] V. V. Atuchin, T. A. Gavrilova, T. I. Grigorieva, N. V. Kuratieva, K. A. Okotrub, N. V. Pervukhina, N. V. Surovtsev, *J. Cryst. Growth* **2011**, 318, 987.
- [57] T. Hirata, K. Ishioka, M. Kitajima, *Appl. Phys. Lett.* **1996**, 68, 458.
- [58] B. X. Wang, S. J. Dong, *J. Electroanal. Chem.* **1994**, 379, 207.
- [59] A. J. Bard, L. R. Faulkner, *Electrochemical Methods: Fundamentals and Applications*, Wiley, New York **2001**.
- [60] J. Z. Ou, J. L. Campbell, D. Yao, W. Wlodarski, K. Kalantar-zadeh, *J. Phys. Chem. C* **2011**, 115, 10757.
- [61] X. K. Hu, Y. T. Qian, Z. T. Song, J. R. Huang, R. Cao, J. Q. Xiao, *Chem. Mater.* **2008**, 20, 1527.
- [62] P. P. Atluri, W. G. Regehr, *J. Neurosci.* **1996**, 16, 5661.
- [63] T. Chang, S. H. Jo, W. Lu, *ACS Nano* **2011**, 5, 7669.
- [64] C. Du, W. Ma, T. Chang, P. Sheridan, W. D. Lu, *Adv. Funct. Mater.* **2015**, 25, 4290.
- [65] R. S. Zucker, W. G. Regehr, *Annu. Rev. Physiol.* **2002**, 64, 355.
- [66] Y. van de Burgt, E. Lubberman, E. J. Fuller, S. T. Keene, G. C. Faria, S. Agarwal, M. J. Marinella, A. A. Talin, A. Salleo, *Nat. Mater.* **2017**, 16, 414.